

Pose2Pose: 3D Positional Pose-Guided 3D Rotational Pose Prediction for Expressive 3D Human Pose and Mesh Estimation

Gyeongsik Moon Kyoung Mu Lee

ECE & ASRI, Seoul National University, Korea
 {mks0601, kyoungmu}@snu.ac.kr



Figure 1: Qualitative results of the proposed Pose2Pose on in-the-wild images. Our framework can produce accurate expressive 3D human pose and mesh, which includes body, hands, and face.

Abstract

Previous 3D human pose and mesh estimation methods mostly rely on only global image feature to predict 3D rotations of human joints (i.e., 3D rotational pose) from an input image. However, local features on the position of human joints (i.e., positional pose) can provide joint-specific information, which is essential to understand human articulation. To effectively utilize both local and global features, we present Pose2Pose, a 3D positional pose-guided 3D rotational pose prediction network, along with a positional pose-guided pooling and joint-specific graph convolution. The positional pose-guided pooling extracts use-

ful joint-specific local and global features. Also, the joint-specific graph convolution effectively processes the joint-specific features by learning joint-specific characteristics and different relationships between different joints. We use Pose2Pose for expressive 3D human pose and mesh estimation and show that it outperforms all previous part-specific and expressive methods by a large margin. The codes will be publicly available.

1. Introduction

Expressive 3D human pose and mesh estimation aims to localize joints and mesh vertices of all human parts, includ-

ing body, hands, and face, simultaneously in the 3D space. By combining 3D pose and mesh of all human parts, we can understand not only human articulation and shape but also human intention and feeling, which can be useful in motion capture, virtual/augmented reality, and human action recognition. This is a very challenging task and has been addressed by only several recent approaches.

Previous 3D human pose and mesh estimation methods [5, 10, 16, 21, 22, 35, 49] mostly rely on only global image feature to predict 3D rotations of human joints (*i.e.*, 3D rotational pose). They perform global average pooling (GAP) on the extracted image feature from ResNet [11] and pass the pooled feature to several fully connected layers for the 3D rotational pose prediction. The estimated 3D rotations are passed to human model layers (*e.g.*, SMPL [26] for body, MANO [36] for hands, FLAME [23] for face, or SMPL-X [33] for all parts) for the final 3D pose and mesh. Although the global image feature can provide overall articulation of human, it lacks joint-specific local information, which can be obtained from features on the position of human joints (*i.e.*, positional pose). However, GAP in their networks breaks the spatial domain; thus, it limits a chance of utilizing the local features on the positional pose.

To effectively utilize both local and global features, we present *Pose2Pose*, a 3D positional pose-guided 3D rotational pose prediction network. Our *Pose2Pose* consists of PositionNet and RotationNet. PositionNet predicts the 3D positional pose from an input image in a fully convolutional way. Then, a positional pose-guided pooling extracts joint-specific local and global features on the predicted positional pose of the ResNet output image feature. From the extracted joint-specific features, the RotationNet constructs a human skeleton graph and regresses the 3D rotational pose using a joint-specific graph convolution. Unlike the vanilla graph convolution [20] that shares learnable weights for all graph vertices, our joint-specific graph convolution uses separated learnable weights for each joint, which share a similar spirit of Liu *et al.* [25]. This joint-specific graph convolution effectively processes the joint-specific local and global features by learning joint-specific characteristics and different relationships between different joints.

We use our *Pose2Pose* for expressive 3D human pose and mesh estimation. The proposed *Pose2Pose* significantly outperforms previous 3D human pose and mesh estimation methods by a large margin. Figure 1 shows qualitative results of the proposed *Pose2Pose*.

Our contributions can be summarized as follows.

- We present *Pose2Pose*, a 3D positional pose-guided 3D rotational pose prediction network for expressive 3D human pose and mesh estimation. Our *Pose2Pose* utilizes joint-specific local and global features, extracted by a positional pose-guided pooling.
- To effectively process joint-specific local and global features, we propose to use a joint-specific graph convolution.
- We show that our *Pose2Pose* outperforms all previous part-specific and expressive 3D human pose and mesh estimation methods.

2. Related works

3D human body pose and mesh estimation. Current 3D human body pose and mesh estimation methods can be categorized into model-based and model-free approaches. The model-based approach predicts human model parameters (*e.g.*, 3D rotations of joints and an identity latent code) and pass the predicted parameters to the human model layers (*e.g.*, SMPL [26]). Kanazawa *et al.* [16] proposed an end-to-end trainable human mesh recovery system that uses the adversarial loss to make their output human shape is anatomically plausible. Pavlakos *et al.* [35] used 2D joint heatmaps and silhouette as cues for predicting accurate SMPL parameters. Omran *et al.* [31] proposed a similar system, which exploits human part segmentation as a cue for regressing SMPL parameters. Kolotouros *et al.* [21] introduced a self-improving system consists of the SMPL parameter regressor and iterative fitting framework [4].

On the other hand, the model-free approach estimates the joints and mesh vertices coordinates. Kolotouros *et al.* [22] designed a GraphCNN, which takes a template human mesh in a rest pose as input and outputs mesh vertices coordinates using image feature from ResNet [11]. Moon and Lee [29] proposed an image-to-lixel prediction network, which predicts three lixel-based 1D heatmaps for each joint or mesh vertex in x -, y -, and z -axis. Choi *et al.* [6] presented a GraphCNN that recovers 3D human mesh vertices coordinates from a 2D human pose.

3D human hand pose and mesh estimation. As the 3D human body pose and mesh estimation, current 3D human hand pose and mesh estimation methods also can be categorized into model-based and model-free approaches. MANO [36] is a widely used human hand model. Baek *et al.* [3] trained their network to estimate the MANO parameters using a differentiable renderer. Boukhayma *et al.* [5] trained their network that takes a single RGB image and estimates MANO parameters by minimizing the distance of the estimated hand joint locations and groundtruth.

On the other hand, several model-free approaches predict hand joints and mesh vertices coordinates. Ge *et al.* [9] proposed a GraphCNN, which directly estimates vertices coordinates of hand mesh from the extracted image feature. Moon and Lee [29] and Choi *et al.* [6] showed their networks also perform well not only on the human body but also on the human hand.

3D human face pose and mesh estimation. Fully super-

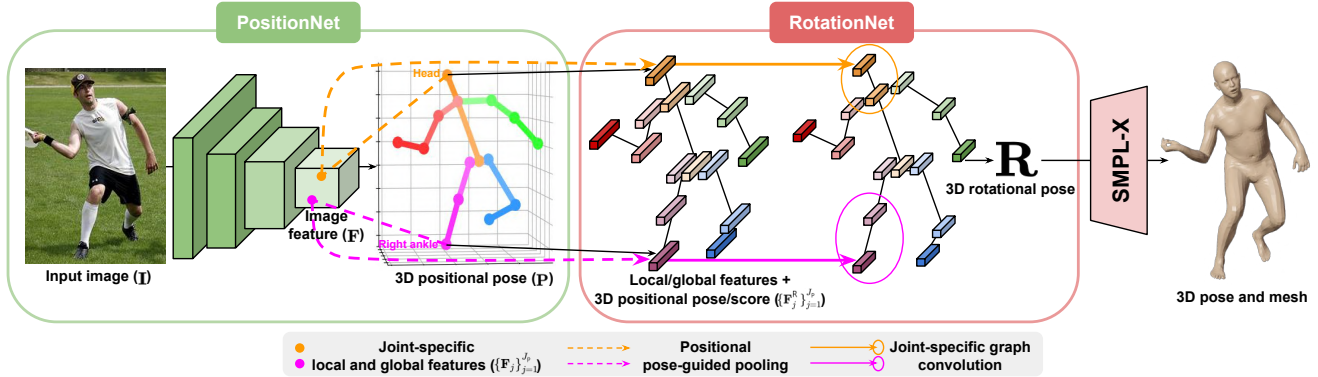


Figure 2: The overall pipeline of Pose2Pose, which consists of PositionNet and RotationNet. The PositionNet predicts the 3D positional pose. Then, the positional pose-guided pooling extracts the joint-specific local and global features. The RotationNet takes the joint-specific features with the 3D positional pose/scores and predicts 3D rotational pose by the joint-specific graph convolution. The final 3D human pose and mesh are obtained by forwarding the predicted 3D human model parameters, including 3D rotational pose to a human model layer (e.g., SMPL-X [33]). For the simplicity, we only illustrated body part Pose2Pose and head and right ankle operations.

vised 3D human face pose and mesh estimation methods require 3D groundtruths to train their networks. Sela *et al.* [40] uses a synthetic dataset to make an image-to-depth mapping and a pixel-to-vertex mapping. The mappings are combined to generate the face mesh. Tran *et al.* [43] fit a 3D morphable model to multiple images of the same subject to generate groundtruth 3D face mesh.

On the other hand, weakly supervised methods only require 2D groundtruths. Tewari *et al.* [42] train their network in an end-to-end manner using a photometric loss and an optional 2D feature loss. Sanyal *et al.* [39] proposed RingNet, which explicitly enforces the identity consistency between the estimated identity codes from the multiple images of the same subject.

Expressive 3D human pose and mesh estimation. Due to its difficulty and absence of the unified expressive body model, there have been very few attempts to simultaneously recover the 3D human pose and mesh of all human parts, including body, hands, and face. Most previous attempts are an optimization-based approach, which fits a 3D human model to the 2D/3D evidence. Joo *et al.* [15] fits their human models (*i.e.*, Frank and Adam) to 3D human joints coordinates and point clouds in a multi-view studio environment. Xiang *et al.* [45] extended Joo *et al.* [15] to the single RGB case. Pavlakos *et al.* [33] and Xu *et al.* [47] fits their human model, SMPL-X and GHUM, respectively, to 2D human joint coordinates. As the above optimization-based methods can be slow and prone to noisy evidence, a regression-based approach is presented recently. Choutas *et al.* [7] presented ExPose, which predicts the expressive human pose and mesh using body-driven attention.

Our Pose2Pose is also the regression-based approach; however, it has a clear difference compared with the previous work, ExPose [7]. ExPose consists of body, hand, and

face branches, and each branch relies on only global image features to regress the parameters of the corresponding human model from the input images. On the other hand, our Pose2Pose exploits both local and global features by the positional pose-guided pooling and joint-specific graph convolution. We show that utilizing both local and global features brings significant performance gain.

Local and global features for 3D human pose and mesh estimation. Utilizing both local and global features has been proven to be crucial for accurate 3D human pose and mesh estimation. Detection-based 3D human pose and mesh estimation methods [28,29,34,41] have achieved high 3D positional pose accuracy by utilizing both local and global features. They *detect* the human joints or mesh vertices from an input image by predicting heatmaps, which have activations where human joints or mesh vertices likely exist. As the heatmap is predicted in a fully convolutional way, the detection-based methods do not require GAP; thus, they can utilize both local and global features. However, their methods are hard to be used to predict 3D rotational pose because the input image only contains the position and intensity of each pixel; thus, the 3D rotational pose cannot be predicted in a fully convolutional way.

On the other hand, regression-based methods [16, 21, 22, 35] can predict both 3D positional and rotational pose by a direct *regression*. However, previous regression-based methods suffer from low accuracy compared with detection-based methods because the previous ones rely only on global features, obtained by GAP.

Our Pose2Pose greatly improves the previous regression-based network by utilizing both local and global features. To this end, we combine the regression-based network with the detection-based network. Our detection-based network, PositionNet, provides the 3D positional pose. Then, we ex-

tract the local and global features on the predicted positional pose of the ResNet output image feature by the positional pose-guided pooling. Our regression-based network, RotationNet, accurately predicts the 3D rotational pose by the joint-specific graph convolution from the local and global features.

3. Pose2Pose

Figure 2 shows the overall pipeline of the proposed Pose2Pose. Pose2Pose consists of PositionNet and RotationNet, which will be described in the following subsections.

3.1. PositionNet

The PositionNet is designed as a fully convolutional network, which predicts 3D positional pose (*i.e.*, 3D positions of human joints) $\mathbf{P} = [\mathbf{p}_1, \dots, \mathbf{p}_{J_p}]^T \in \mathbb{R}^{J_p \times 3}$ from an input image \mathbf{I} . J_p denotes the number of joints representing the 3D positional pose. x - and y -axis of \mathbf{P} are defined in image space, and z -axis of it is defined in root joint (*i.e.*, pelvis for the body and wrist for the hand)-relative depth space. For this, PositionNet extracts image feature $\mathbf{F} \in \mathbb{R}^{C \times H \times W}$ from the input image by ResNet [11], where C , H , and W denote the number of channels, height, and width. Then, a 1-by-1 convolution predicts 3D heatmaps of human joints $\mathbf{H} \in \mathbb{R}^{J_p \times D \times H \times W}$, where D denotes the depth dimension size. To predict the 3D heatmaps from the 2D feature map \mathbf{F} , the 1-by-1 convolution first predicts a tensor of shape $\mathbb{R}^{J_p \times D \times H \times W}$, and we reshape the tensor to the shape of \mathbf{H} following Sun *et al.* [41]. The 3D positional pose \mathbf{P} is calculated from \mathbf{H} by the soft-argmax operation [41] in a differentiable way.

3.2. RotationNet

The RotationNet is designed as a graph convolutional network (GraphCNN), which predicts the 3D rotational pose (*i.e.*, 3D rotations of human joints) $\mathbf{R} \in \mathbb{R}^{J_r \times 3}$, as illustrated in Figure 3. J_r denotes the number of joints representing the 3D rotational pose, which is often different from J_p . To this end, we construct a graph $\mathcal{G} = (\mathcal{V}, \mathbf{A})$, where \mathcal{V} and \mathbf{A} are graph vertices and an adjacency matrix, respectively. The graph vertices represent human joints, where $|\mathcal{V}| = J_p$. The adjacency matrix $\mathbf{A} \in \{0, 1\}^{J_p \times J_p}$ is constructed based on the human skeleton hierarchy in a pre-processing stage and fixed during the training and testing stage.

The initial feature of a j th graph vertex $\mathbf{F}_j^R \in \mathbb{R}^{C+4}$ is a concatenation of a joint-specific local and global feature $\mathbf{F}_j \in \mathbb{R}^C$, the predicted 3D positional pose of j th joint $\mathbf{p}_j \in \mathbb{R}^3$, and 3D positional pose prediction confidence of j th joint $c_j \in \mathbb{R}$. The joint-specific features provide semantic information to the graph, computed by the positional

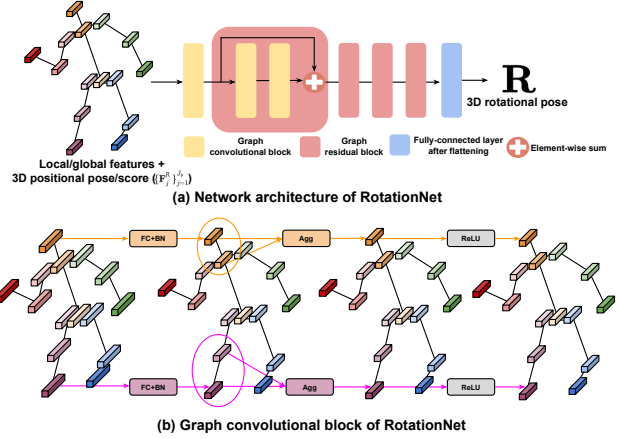


Figure 3: (a) The network architecture of the RotationNet. (b) The pipeline of the graph convolutional block, which processes graph features by the joint-specific graph convolution and aggregates the graph features using the adjacency matrix. FC, BN, and Agg denote a fully connected layer, 1D batch normalization, and graph feature aggregation using the adjacency matrix, respectively. We visualize detailed operations of only head and right ankle for the simplicity.

pose-guided pooling. Moreover, the 3D positional pose provides geometric evidence, which conveys essential human articulation information. Finally, the prediction confidence can tell whether the joint-specific image feature and the 3D positional pose of each joint are reliable or not. The initial features of all graph vertices $\{\mathbf{F}_j^R\}_{j=1}^{J_p}$ are processed by the joint-specific graph convolution. We provide detailed descriptions of the positional pose-guided pooling and joint-specific graph convolution below.

Positional pose-guided pooling. The positional pose-guided pooling computes joint-specific local and global features $\{\mathbf{F}_j\}_{j=1}^{J_p}$ using the predicted 3D positional pose \mathbf{P} . Since the coordinates of \mathbf{p}_j , (x_j, y_j) are not integers, we obtain the j th joint feature \mathbf{F}_j at position \mathbf{p}_j using bilinear interpolation on the image feature map \mathbf{F} . The interpolated feature \mathbf{F}_j is obtained from the exact position of the joint j ; thus, it contains a local feature. However, the interpolated feature is not restricted to the local feature because the large size of the receptive field of ResNet output makes \mathbf{F}_j contain information around the position of joint j , as well. Thus, \mathbf{F}_j contains both joint-specific local and global features. The 3D positional pose prediction confidences $\{c_j\}_{j=1}^{J_p}$ are also obtained by performing the positional pose-guided pooling on the estimated 3D heatmap \mathbf{H} .

Joint-specific graph convolution. Our joint-specific graph convolution uses separated learnable weights for each graph vertex. Specifically, we define learnable weight matrices $\{W_j \in \mathbb{R}^{C_{out} \times C_{in}}\}_{j=1}^{J_p}$ for all joints of each graph convolution layer, where C_{in} and C_{out} denotes input and output channel dimensions, respectively. Then, the out-

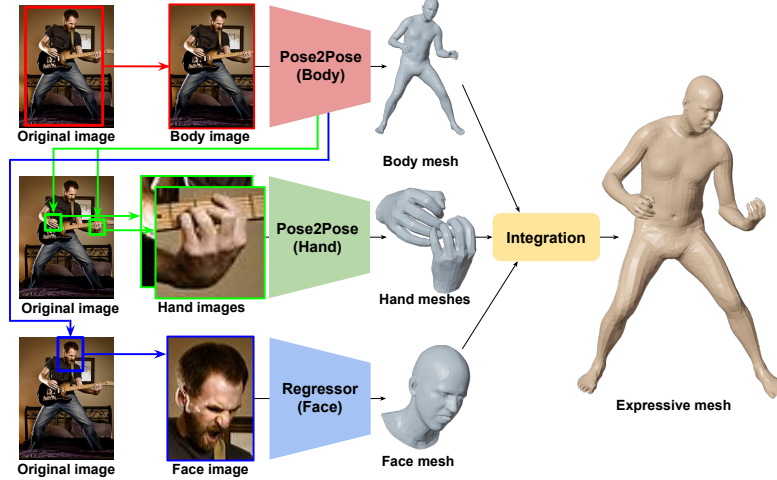


Figure 4: Our entire system for expressive 3D human pose and mesh estimation consists of three separated networks for the body, hand, and face. In the testing stage, the hand/face images are obtained using the predicted hand/face boxes from the body part. The integration module integrates the outputs of the three networks.

put graph feature of joint j is obtained by $\mathbf{F}_j^{\text{out}} = \sigma_{\text{ReLU}}(\sum_{i \in \hat{\mathcal{N}}_j} \tilde{a}_{ji} \sigma_{\text{BN}}(W_i \mathbf{F}_i^{\text{in}}))$, where \mathbf{F}_i^{in} is the input graph feature of joint i . σ_{ReLU} and σ_{BN} denotes ReLU activation function and 1D batch normalization [12], respectively. $\hat{\mathcal{N}}_j$ is defined as $\mathcal{N}_j \cup \{j\}$, where \mathcal{N}_j denotes neighbors of a vertex j . \tilde{a}_{ji} is an entry of the normalized adjacency matrix $\tilde{\mathbf{A}}$ at (j, i) , where $\tilde{\mathbf{A}} = \mathbf{D}^{-\frac{1}{2}}(\mathbf{A} + \mathbf{I})\mathbf{D}^{-\frac{1}{2}}$. \mathbf{D} is a diagonal matrix of $\mathbf{A} + \mathbf{I}$. The RotationNet follows the network architecture of Liu *et al.* [25], which consists of one graph convolutional block and four graph residual blocks. Each block consists of joint-specific graph convolution, 1D batch normalization, and ReLU activation function. All the graph features have a channel dimension of 128, except for that of the input and output features.

At the last part of the RotationNet, we flatten the graph features into a vector and use a single fully connected layer to predict 3D rotational pose \mathbf{R} .

4. Expressive 3D human pose and mesh estimation

For the expressive 3D human pose and mesh estimation, we construct three separate networks for the body, hand, and face following Choutas *et al.* [7], as shown in Figure 4. This separation enables us to use part-specific datasets such as FreiHAND [49] and FFHQ [18]. Each network is responsible for each part, and an integration module integrates outputs of each network in the testing stage. We provide descriptions of the networks of each part and the integration module below.

4.1. Body part

The body part uses Pose2Pose to predict 3D body global rotation $\theta_b^g \in \mathbb{R}^3$, 3D body rotational pose $\theta_b \in \mathbb{R}^{21 \times 3}$,

shape parameter $\beta_b \in \mathbb{R}^{10}$, and camera parameter $k_b \in \mathbb{R}^3$. θ_b^g and θ_b are predicted from RotationNet, and β_b and k_b are predicted from the global average pooled \mathbf{F} using a separated fully connected layer. Instead of directly predicting θ_b , we initially predict a latent code of VPoser [33] z_b and use VPoser to decode z_b to θ_b . The outputs are passed to the SMPL-X layer to obtain the final 3D body pose and mesh.

The body part additionally predicts hand and face bounding boxes to make the hand and face-cropped images during the testing stage. To this end, we concatenate the image feature \mathbf{F} and 2D heatmap \mathbf{H}' and pass it to two convolutional layers. The 2D heatmap \mathbf{H}' is generated by making a Gaussian blob on the (x, y) position of \mathbf{P} . The soft-argmax [41] is applied to the output of the convolutional layers for the box centers. The widths and heights of the boxes are computed by performing positional pose-guided pooling on the box centers of \mathbf{F} and pass the features of each box center to separated fully connected layers.

4.2. Hand part

We use exactly the same network architecture like that of the body part. The hand part outputs 3D hand global rotation $\theta_h^g \in \mathbb{R}^3$, 3D hand rotational pose $\theta_h \in \mathbb{R}^{15 \times 3}$, shape parameter $\beta_h \in \mathbb{R}^{10}$, and camera parameter $k_h \in \mathbb{R}^3$. The outputs are passed to the MANO layer to obtain the final 3D hand pose and mesh.

4.3. Face part

Unlike the joints of the body and hand, most of the face keypoints do not move according to 3D rotations of joints, making it hard to apply Pose2Pose. Instead, we design a simple regressor that consists of ResNet and fully connected layers. We perform GAP on the image feature \mathbf{F} and fed it to separated fully connected layers, which predict 3D face

global rotation $\theta_f^g \in \mathbb{R}^3$, 3D jaw rotation $\theta_f \in \mathbb{R}^3$, shape parameter $\beta_f \in \mathbb{R}^{10}$, and expression code $\psi \in \mathbb{R}^{10}$. The predicted parameters are passed to the FLAME layer to obtain the final 3D face pose and mesh.

4.4. Training the networks

The three networks of each part are trained separately. For all parts, we calculate $L1$ loss between predicted and groundtruth 3D positional pose following Moon and Lee [29]. In addition, $L1$ loss between predicted and groundtruth SMPL-X/MANO/FLAME parameters, 3D joint coordinates of SMPL-X/MANO/FLAME, and projected 2D joint coordinates are also calculated following Kolotouros [21]. For the hand and face box localization, we calculate $L1$ loss between predicted and groundtruth box centers, widths, and heights.

4.5. Integration of all parts in the testing stage

The final expressive 3D human pose and mesh is obtained by forwarding $\{\theta_b^g, \theta_b, \beta_b, \theta_{rh}^g, \theta_{rh}, \theta_{lh}^g, \theta_{lh}, \theta_f, \psi\}$ to SMPL-X, where $*_{rh}$ and $*_{lh}$ denote $*$ is from right and left hand, respectively. The 3D hand pose parameter θ_h of MANO and 3D jaw rotation θ_f and face expression code ψ of FLAME are compatible with those of SMPL-X; thus, we use them for the final prediction. As the body part often predicts wrong rotations of elbows and wrists in the roll axis, we selectively use the 3D hand global rotation θ_h^g to replace rotations of the elbows and wrists based on a simple thresholding. The thresholding assumes rotations of elbows and wrists in the roll axis are almost the same, which follows the anatomical structure of the human body. We provide detailed descriptions of the thresholding in the supplementary material.

5. Implementation details

PyTorch [32] is used for implementation. The backbone part is initialized with the publicly released ResNet50 [11] pre-trained on ImageNet [38]. The weights are updated by Adam optimizer [19] with a mini-batch size of 192. The human body region is cropped using groundtruth box in both of training and testing stages following previous works [16, 21, 22]. The hand and face images are cropped from the original image using groundtruth box in the training stage and the predicted box in the testing stage. The cropped image is resized to 256×256 . Data augmentations, including scaling, rotation, random horizontal flip, and color jittering, are performed in training. All the 3D rotations except for θ_b are initially predicted in the 6D rotational representation of Zhou *et al.* [48] and converted to the 3D axis-angle rotations. We flipped all hands to the right hand during the training and testing stage of the hand part. The initial learning rate is set to 10^{-4} and reduced by a factor of 10 at the 10th epoch. We train each body, hand, and

How to pool?	How to process?	PA MPJPE
GAP	FC	60.7 [16, 21, 35]
	GraphCNN	59.5
GAP+PPP	FC	57.4
	GraphCNN	57.6
PPP	FC	57.5
	GraphCNN	56.8 (Ours)

Table 1: PA MPJPE comparison between models with various pooling methods and processing modules on 3DPW.

face part separately for 12 epochs with four NVIDIA RTX 2080 Ti GPUs.

6. Experiment

6.1. Training sets and evaluation metrics

Training sets. To train the body part, we use Human3.6M [13], MPI-INF-3DHP [27], MSCOCO [14, 24], and MPII [1]. For the hand part, FreiHAND [49], InterHand2.6M [30], and MSCOCO [14] are used for the training. Finally, FFHQ [18] and MSCOCO [14] are used for the face part training. We obtained SMPL/SMPL-X/MANO/FLAME fits of the datasets using SMPLify-X [33] and used them as pseudo-groundtruths. We will release all fits for the reproducible and continual study.

Evaluation metrics. MPJPE and MPVPE are widely used to evaluate 3D human body/hand pose and mesh estimation, where each calculates the average 3D joint distance (mm) and 3D mesh vertex distance (mm) between predicted and groundtruth, respectively, after aligning a root joint translation. PA MPJPE and PA MPVPE further align a rotation and scale. F-score is additionally used for the 3D hand pose and mesh estimation evaluation. For the face part, the average of the closest distance between a predicted 3D face mesh vertex and groundtruth 3D face scan point is used.

6.2. Ablation study

For the ablation study, we train the body part on Human3.6M, MSCOCO, and MPII and report errors on 3DPW, which is a standard experimental protocol of recent 3D human body pose and mesh estimation works. We use SMPL for the human model of the body part. The same tendency of the ablation study was observed for the hand part.

Effectiveness of the positional pose-guided pooling. We show the effectiveness of the positional pose-guided pooling (PPP) in Table 1. For this, we report PA MPJPE of our Pose2Pose and its variants that use GAP or a combination of GAP and PPP. As the table shows, adding PPP to GAP or replacing GAP with PPP decrease the error regardless of the processing modules, fully connected layer (FC) and GraphCNN. It is noticeable that our PPP achieves significantly lower error compared with the combination of GAP and FC, the most widely used one in previous

How to pool?	Which graph conv.?	PA MPJPE
GAP	Shared graph conv.	61.5 [22]
	Joint-specific graph conv.	59.5
PPP	Shared graph conv.	64.5
	Joint-specific graph conv.	56.8 (Ours)

Table 2: PA MPJPE comparison between models with various pooling methods and graph convolutions on 3DPW.

Image feature	Joint coordinate + confidence	PA MPJPE
✓	✗	58.0
✗	✓	59.2
✓	✓	56.8 (Ours)

Table 3: PA MPJPE comparison between models with various input combinations of the RotationNet.

works [16, 21, 35]. Interestingly, replacing GAP with PPP achieves a better result than adding PPP to GAP when the GraphCNN is used. This is because a global image feature from the GAP contains much unnecessary information, such as backgrounds, which makes the performance worse. On the other hand, the local and global features from the PPP contains essential human articulation information, and the GraphCNN aggregates the features by considering the human skeleton hierarchy, which makes the aggregated feature highly useful. The comparisons clearly show the benefit of PPP, which preserves joint-specific local and global features, while GAP cannot. For the experiment, we used the joint-specific graph convolution for all GraphCNN. When PPP is used, the local and global image features of joints and joint coordinates with the confidence are used for the final 3D rotational pose prediction.

Effectiveness of the joint-specific graph convolution. Table 2 shows the benefit of the joint-specific graph convolution. To this end, we report PA MPJPE of Pose2Pose and its variants that use GAP or the shared graph convolution. The shared graph convolution uses shared learnable weights for all graph vertices like the vanilla graph convolution [20]. Our joint-specific graph convolution achieves a lower error than the shared graph convolution regardless of the pooling method, GAP and PPP. Especially, the combination of the PPP and the joint-specific graph convolution significantly outperforms a combination of GAP and shared graph convolution, used in Kolotouros *et al.* [22]. We also found that the shared graph convolution increases the error a lot when the input features are from PPP. This is because the shared graph convolution applies the same weights to features of all graph vertices, while each feature of a graph vertex from PPP has distinctive joint-specific information. The comparisons clearly show the benefit of the joint-specific graph convolution.

Inputs of the RotationNet. We show how each input of the RotationNet affects the accuracy in Table 3. The table shows that taking both the image feature and joint coordi-

Methods	Scale	MPJPE	PA MPJPE	
HMR [16]	Body only	130.0	81.3	
HMMR [17]		-	72.6	
GraphCMR [22]		-	70.2	
Arnab <i>et al.</i> [2]		-	72.2	
SPIN [21]		96.9	59.2	
Pose2Mesh [6]		88.9	58.3	
I2L-MeshNet [29]		93.2	57.7	
ExPose [7]		All parts	93.4	60.7
Pose2Pose (Ours)			89.4	55.5

Table 4: MPJPE and PA MPJPE comparison on 3DPW.

Methods	Scale	PA errors	F scores
Hasson <i>et al.</i> [10]	Hand only	13.2 / -	0.436 / 0.908
Boukhayma <i>et al.</i> [5]		13.0 / -	0.435 / 0.898
FreiHAND [49]		10.7 / -	0.529 / 0.935
Pose2Mesh [6]		7.8 / 7.7	0.674 / 0.969
I2L-MeshNet [29]		7.6 / 7.4	0.681 / 0.973
ExPose [7]		All parts	11.8 / 12.2
Pose2Pose (Ours)	7.4 / 7.4		0.683 / 0.974

Table 5: PA MPVPE/PA MPJPE and F-score@5mm/15mm comparison on FreiHAND.

Methods	Scale	Mean	Median	Std.
RingNet [39]	Face only	2.08/2.02	1.63/1.58	1.79/ 1.68
ExPose [7]	All parts	2.27/2.42	1.76/1.91	1.97/2.03
Regressor (Ours)		2.02/1.99	1.55/1.53	1.78/1.76

Table 6: Mean, median, and standard deviation of 3D face mesh error comparison on low-quality/high-quality images of Stirling.

nate with confidence achieves the best accuracy. The image feature extracted by PPP can provide local/global contextual information, and the joint coordinate with confidence predicted by PositionNet can provide 3D geometric information. We design our RotationNet to take both inputs, thus can utilize both local/global contextual information and 3D geometric information. The comparison clearly shows the validity of our RotationNet design.

6.3. Comparison with state-of-the-art methods

Body part. Table 4 shows comparison between our body part Pose2Pose and previous state-of-the-art methods on 3DPW [44]. It shows our Pose2Pose significantly outperforms previous works by a large margin, including both body-only methods and the expressive method [7]. Following previous works [6, 21, 29], we use SMPL for the human model, and 14 joints are used for the evaluation.

Hand part. Table 5 shows a comparison between our hand part Pose2Pose and previous state-of-the-art methods on FreiHAND [49]. It shows our Pose2Pose achieves comparable accuracy with a recent state-of-the-art hand-only method [29] and significantly outperforms the expressive



Figure 5: Qualitative results of our framework on MSCOCO.

Methods	PA MPVPE			PA MPJPE	
	All	Hands	Face	Body	Hands
SMPLify-X [33]	65.3	12.3	6.3	87.6	12.9
MTC [45]	67.2	-	-	107.8	16.7
ExPose [7]	54.5	12.8	5.8	62.8	13.1
Pose2Pose (Ours)	51.9	12.0	5.6	62.6	11.8

Table 7: PA MPVPE and PA MPJPE comparison on EHF. The numbers in hands are averaged values of left and right hands.

method [7].

Face part. Table 6 shows comparison between our face part regressor and previous state-of-the-art methods on Stirling [8]. It shows our regressor achieves lower errors compared with the face-only method and expressive method [7]. **All parts.** Table 7 shows comparison between our Pose2Pose and previous expressive methods on EHF [33]. SMPL-X is used for the human model of the body part. For the evaluation, we integrated body, hand, and face parameters by our integration module, described in Section 4.5. The table shows our Pose2Pose outperforms previous methods by a large margin.

Taken together, our Pose2Pose outperforms all methods on all part-specific and expressive datasets. The comparisons clearly show the effectiveness of Pose2Pose, benefit from our novel positional pose-guided pooling and joint-

specific graph convolution. Figure 5 shows qualitative results of Pose2Pose on MSCOCO.

6.4. Running time

From a single RGB image, the body and hand part Pose2Pose take 0.06 and 0.07 seconds per frame, respectively, and the face regressor takes 0.02 seconds per frame. The hand part takes the left and right hand images simultaneously. The integration module takes 0.01 seconds per frame, which includes the forwarding time to the SMPL-X layer. In total, our whole framework runs at 6.3 frames per second for expressive 3D human pose and mesh estimation from a single RGB image. This is the same running time as that of the previous expressive method, ExPose [7]. The running times are measured by using a single RTX 2080 Ti GPU and making the mini-batch size 1.

7. Conclusion

We present Pose2Pose, a 3D positional pose-guided 3D rotational pose prediction network for expressive 3D human pose and mesh estimation from a single RGB image. In contrast to previous works that rely on only global image feature, ours utilize joint-specific local and global features, extracted by the positional pose-guided pooling, with joint-specific graph convolution. We apply our Pose2Pose for ex-

pressive 3D human pose and mesh estimation and achieved state-of-the-art accuracy on all part-specific and expressive datasets.

Supplementary Material of “Pose2Pose: 3D Positional Pose-Guided 3D Rotational Pose Prediction for Expressive 3D Human Pose and Mesh Estimation”

In this supplementary material, we present more experimental results that could not be included in the main manuscript due to the lack of space.

Algorithm 1 Integration of body and hands

Input: θ_b^g : Global rotation of body
Input: $\theta_b = \{\theta_j^l\}_{j=1}^{21}$: Local rotations of body joints
Input: $\theta_{rh}^g, \theta_{lh}^g$: Global rotations of right and left hands
Output: θ_b : Updated local rotations of body joints

- 1: Compute global rotations of body joints $\{\theta_j^g\}_{j=1}^{21}$ from θ_b^g and θ_b by forward kinematics
- 2: Let re, le, rw, lw denote joint index of right elbow, left elbow, right wrist, and left wrist, respectively.
- 3: **for** $(e, w, h) \leftarrow ((re, rw, rh), (le, lw, lh))$ **do**
- 4: $\theta_w^g \leftarrow \theta_h^g$
- 5: x -axis of $\theta_e^g \leftarrow x$ -axis of $(\theta_e^g + \theta_h^g)/2$
- 6: Compute new local rotations of elbow and wrist, $\hat{\theta}_e^l$ and $\hat{\theta}_w^l$, respectively, from $\{\theta_j^g\}_{j=1}^{21}$ by reversing forward kinematics
- 7: **if** $|y$ -axis of $\hat{\theta}_w^l| < \pi/4$ and $|z$ -axis of $\hat{\theta}_w^l| < \pi/2$ **then**
- 8: Update $\theta_w^l \leftarrow \hat{\theta}_w^l$
- 9: Update $\theta_e^l \leftarrow \hat{\theta}_e^l$
- 10: **end if**
- 11: **end for**

8. All parts integration module

As described in Section 4.5, we selectively use global rotations of right and left hands, θ_{rh}^g and θ_{lh}^g , respectively, when integrating outputs of networks of each part. Algorithm 1 and Figure 6 show the integration procedure and how rotations of elbow and wrist change the body, respectively. First, we perform forward kinematics to compute global rotations of all body joints, including wrists and elbows (line 1). Then, we replace the global rotations of wrists and elbows using the global rotation of hands (lines 4 and 5). The replacement assumes x -axis rotations (roll of Euler angle) of the wrist and elbow are almost the same, which follows the anatomical structure of the human body, as shown in Figure 6. To avoid a sudden change of the elbow rotation, which can cause artifacts, we use an average rotation of the elbow and wrist (line 5). From the replaced global rotations of wrists and elbows, we compute new local rotations of wrists and elbows (line 6). Finally, we check the new local rotation follows the anatomical structure of the human body (line 7), where y - and z -axis rotations are

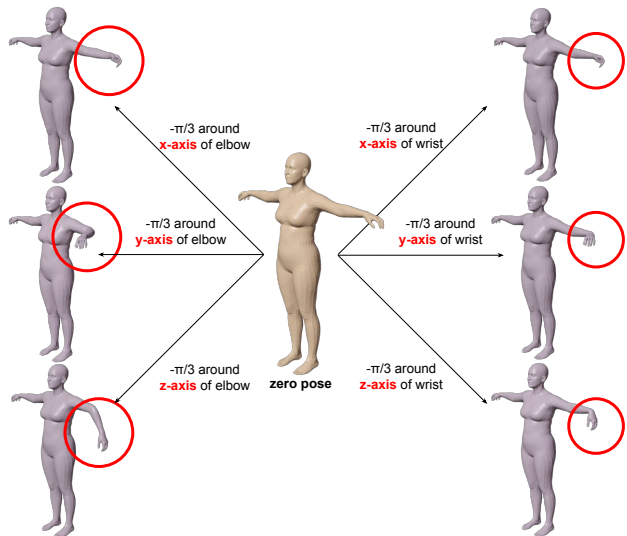


Figure 6: Visualized rotations of the elbow and wrist in each axis.

shown in Figure 6. If true, we update the local rotations of body joints, which become the final output of the integration (lines 8 and 9). We convert the 3D rotation of joints to Euler angles in line 3 - line 11. The integration is only performed when the distance between the center of the hand box and predicted wrist position is smaller than the box scale. If the distance is longer than the threshold, we consider the hand is not detected. In that case, we ignore all outputs from the hand part Pose2Pose by skipping Algorithm 1 and setting the hand pose to zero.

9. Effect of PositionNet

We show the effect of the PositionNet on the overall 3D pose accuracy in Table 8. To this end, we initialize ResNet of PositionNet with SimpleBaseline [46], pre-trained on 2D body keypoint of MSCOCO [24], instead of using weights pre-trained on ImageNet. As the table shows, initializing the ResNet with the pre-trained 2D human pose estimation network significantly improves the accuracy. This is because the pre-trained 2D human pose estimation network already can provide accurate 2D pose; thus, it can converge to a better 3D positional pose estimation network. This shows better PositionNet can lead to significant performance gain in our framework.

10. Hand and face box localization evaluation

We provide intersection over union (IoU) of hand and face bounding boxes, predicted by the body part Pose2Pose, in Table 9. As the table shows, ours is good at localizing the face; however, the IoU of the hand part is much lower than that of the face part. Most of the human pose estimation

Methods	MPJPE	PA MPJPE
HMR [16]	130.0	81.3
HMMR [17]	-	72.6
GraphCMR [22]	-	70.2
Arnab <i>et al.</i> [2]	-	72.2
SPIN [21]	96.9	59.2
Pose2Mesh [6]	88.9	58.3
I2L-MeshNet [29]	93.2	57.7
ExPose [7]	93.4	60.7
Pose2Pose (Ours)	89.4	55.5
Pose2Pose*	84.8	52.9

Table 8: MPJPE and PA MPJPE comparison on 3DPW. * denotes its ResNet is from pre-trained SimpleBaseline [46]

Metric	Hand	Face
IoU	0.54	0.77

Table 9: IoU of the hand and face box on MSCOCO validation set. The number of the hand is an averaged number of the right and left hands.

How to pool?	How to process?	PA MPJPE	PA MPVPE
GAP	FC	6.7	6.5
PPP	GraphCNN	5.4	5.2

Table 10: PA MPJPE and PA MPVPE comparison between the previous widely used approach (first row) [5, 10, 37, 49] and our approach (second row) on FreiHAND.

methods have difficulty in accurately localizing hands because of occlusions, small size, and large movement, which should be addressed in future work.

11. Ablation study on hand part

We showed the effectiveness of the positional pose-guided pooling (PPP) and joint-specific graph convolution compared with the previous widely used approach (*i.e.*, a combination of GAP and FC) in Table 1. As the table only provided the body part results, we additionally provide hand part results on FreiHAND [49] in Table 10. Like the results of the body part, our approach (second row) achieves significantly better accuracy compared with the previous widely used approach [5, 10, 37, 49] (first row) in the hand part. The comparison shows our approach, a combination of PPP and joint-specific graph convolution, is highly beneficial for both the human body and hand cases.

For the experiment, we split the FreiHAND training set into training and validation sets and report the results on the validation set. The validation set is randomly sampled at one-tenth of the original training set.

12. Qualitative results on internet images

Figure 7 shows qualitative results on internet images. Our Pose2Pose can generalize well to many unseen im-

ages with various body/hand poses and facial expressions. However, we observed several failure cases. For example, Pose2Pose suffers from depth ambiguity on images with hands close to the body or face. The 2D locations of the hands are correct, but the hands do not touch the body or face. We think this is due to the lack of training data that contain such situations, which should be addressed in future works.



Figure 7: Qualitative results on internet images. From top to bottom, left to right, the persons in the images are Freddie Mercury of band Queen, Lady Gaga, Adele, Dave Mustaine of band Megadeth, James Hetfield of band Metallica, David Draiman of band Disturbed, Lisa Su of AMD, Jensen Huang of NVIDIA, Steven Ogg of GTA 5, Steven Jobs of Apple, Elon Musk of Tesla, and Mark Zuckerberg of Facebook.

References

- [1] Mykhaylo Andriluka, Leonid Pishchulin, Peter Gehler, and Bernt Schiele. 2D human pose estimation: New benchmark and state of the art analysis. In *CVPR*, 2014. 6
- [2] Anurag Arnab, Carl Doersch, and Andrew Zisserman. Exploiting temporal context for 3D human pose estimation in the wild. In *CVPR*, 2019. 7, 11
- [3] Seungryul Baek, Kwang In Kim, and Tae-Kyun Kim. Pushing the envelope for RGB-based dense 3D hand pose estimation via neural rendering. *CVPR*, 2019. 2
- [4] Federica Bogo, Angjoo Kanazawa, Christoph Lassner, Peter Gehler, Javier Romero, and Michael J Black. Keep it SMPL: Automatic estimation of 3D human pose and shape from a single image. *ECCV*, 2016. 2
- [5] Adnane Boukhayma, Rodrigo de Bem, and Philip HS Torr. 3D hand shape and pose from images in the wild. *CVPR*, 2019. 2, 7, 11
- [6] Hongsuk Choi, Gyeongsik Moon, and Kyoung Mu Lee. Pose2Mesh: Graph convolutional network for 3D human pose and mesh recovery from a 2D human pose. *ECCV*, 2020. 2, 7, 11
- [7] Vasileios Choutas, Georgios Pavlakos, Timo Bolkart, Dimitrios Tzionas, and Michael J Black. Monocular expressive body regression through body-driven attention. *ECCV*, 2020. 3, 5, 7, 8, 11
- [8] Zhen-Hua Feng, Patrik Huber, Josef Kittler, Peter Hancock, Xiao-Jun Wu, Qijun Zhao, Paul Koppen, and Matthias Ratsch. Evaluation of dense 3D reconstruction from 2D face images in the wild. *FG*, 2018. 8
- [9] Lihao Ge, Zhou Ren, Yuncheng Li, Zehao Xue, Yingying Wang, Jianfei Cai, and Junsong Yuan. 3D hand shape and pose estimation from a single RGB image. *CVPR*, 2019. 2
- [10] Yana Hasson, Gul Varol, Dimitrios Tzionas, Igor Kalevatykh, Michael J Black, Ivan Laptev, and Cordelia Schmid. Learning joint reconstruction of hands and manipulated objects. *CVPR*, 2019. 2, 7, 11
- [11] Kaifeng He, Xiangyu Zhang, Shaoqing Ren, and Jian Sun. Deep residual learning for image recognition. *CVPR*, 2016. 2, 4, 6
- [12] Sergey Ioffe and Christian Szegedy. Batch Normalization: Accelerating deep network training by reducing internal covariate shift. *ICML*, 2015. 5
- [13] Catalin Ionescu, Dragos Papava, Vlad Olaru, and Cristian Sminchisescu. Human3.6M: Large scale datasets and predictive methods for 3D human sensing in natural environments. *TPAMI*, 2014. 6
- [14] Sheng Jin, Lumin Xu, Jin Xu, Can Wang, Wentao Liu, Chen Qian, Wanli Ouyang, and Ping Luo. Whole-body human pose estimation in the wild. *ECCV*, 2020. 6
- [15] Hanbyul Joo, Tomas Simon, and Yaser Sheikh. Total capture: A 3D deformation model for tracking faces, hands, and bodies. In *CVPR*, 2018. 3
- [16] Angjoo Kanazawa, Michael J Black, David W Jacobs, and Jitendra Malik. End-to-end recovery of human shape and pose. *CVPR*, 2018. 2, 3, 6, 7, 11
- [17] Angjoo Kanazawa, Jason Y Zhang, Panna Felsen, and Jitendra Malik. Learning 3D human dynamics from video. In *CVPR*, 2019. 7, 11
- [18] Tero Karras, Samuli Laine, and Timo Aila. A style-based generator architecture for generative adversarial networks. In *CVPR*, 2019. 5, 6
- [19] Diederik P Kingma and Jimmy Ba. Adam: A method for stochastic optimization. *ICLR*, 2014. 6
- [20] Thomas N Kipf and Max Welling. Semi-supervised classification with graph convolutional networks. *ICLR*, 2017. 2, 7
- [21] Nikos Kolotouros, Georgios Pavlakos, Michael J Black, and Kostas Daniilidis. Learning to reconstruct 3D human pose and shape via model-fitting in the loop. *ICCV*, 2019. 2, 3, 6, 7, 11
- [22] Nikos Kolotouros, Georgios Pavlakos, and Kostas Daniilidis. Convolutional mesh regression for single-image human shape reconstruction. *CVPR*, 2019. 2, 3, 6, 7, 11
- [23] Tianye Li, Timo Bolkart, Michael J Black, Hao Li, and Javier Romero. Learning a model of facial shape and expression from 4D scans. *ACM TOG*, 2017. 2
- [24] Tsung-Yi Lin, Michael Maire, Serge Belongie, James Hays, Pietro Perona, Deva Ramanan, Piotr Dollar, and C Lawrence Zitnick. Microsoft COCO: Common objects in context. In *ECCV*, 2014. 6, 10
- [25] Kenkun Liu, Rongqi Ding, Zhiming Zou, Le Wang, and Wei Tang. A comprehensive study of weight sharing in graph networks for 3D human pose estimation. In *ECCV*, 2020. 2, 5
- [26] Matthew Loper, Naureen Mahmood, Javier Romero, Gerard Pons-Moll, and Michael J Black. SMPL: A skinned multi-person linear model. *ACM TOG*, 2015. 2
- [27] Dushyant Mehta, Helge Rhodin, Dan Casas, Pascal Fua, Oleksandr Sotnychenko, Weipeng Xu, and Christian Theobalt. Monocular 3D human pose estimation in the wild using improved cnn supervision. In *3DV*, 2017. 6
- [28] Gyeongsik Moon, Ju Yong Chang, and Kyoung Mu Lee. V2V-PoseNet: Voxel-to-Voxel prediction network for accurate 3D hand and human pose estimation from a single depth map. *CVPR*, 2018. 3
- [29] Gyeongsik Moon and Kyoung Mu Lee. I2L-MeshNet: Image-to-Lixel prediction network for accurate 3D human pose and mesh estimation from a single RGB image. *ECCV*, 2020. 2, 3, 6, 7, 11
- [30] Gyeongsik Moon, Shou-I Yu, He Wen, Takaaki Shiratori, and Kyoung Mu Lee. InterHand2.6M: A dataset and baseline for 3D interacting hand pose estimation from a single RGB image. *ECCV*, 2020. 6
- [31] Mohamed Omran, Christoph Lassner, Gerard Pons-Moll, Peter Gehler, and Bernt Schiele. Neural Body Fitting: Unifying deep learning and model based human pose and shape estimation. *3DV*, 2018. 2
- [32] Adam Paszke, Sam Gross, Soumith Chintala, Gregory Chanan, Edward Yang, Zachary DeVito, Zeming Lin, Alban Desmaison, Luca Antiga, and Adam Lerer. Automatic differentiation in pytorch. 2017. 6

- [33] Georgios Pavlakos, Vasileios Choutas, Nima Ghorbani, Timo Bolkart, Ahmed AA Osman, Dimitrios Tzionas, and Michael J Black. Expressive body capture: 3D hands, face, and body from a single image. *CVPR*, 2019. 2, 3, 5, 6, 8
- [34] Georgios Pavlakos, Xiaowei Zhou, Konstantinos G Derpanis, and Kostas Daniilidis. Coarse-to-fine volumetric prediction for single-image 3D human pose. In *CVPR*, 2017. 3
- [35] Georgios Pavlakos, Luyang Zhu, Xiaowei Zhou, and Kostas Daniilidis. Learning to estimate 3D human pose and shape from a single color image. *CVPR*, 2018. 2, 3, 6, 7
- [36] Javier Romero, Dimitrios Tzionas, and Michael J Black. Embodied Hands: Modeling and capturing hands and bodies together. *ACM TOG*, 2017. 2
- [37] Yu Rong, Takaaki Shiratori, and Hanbyul Joo. FrankMocap: Fast monocular 3D hand and body motion capture by regression and integration. *arXiv preprint arXiv:2008.08324*, 2020. 11
- [38] Olga Russakovsky, Jia Deng, Hao Su, Jonathan Krause, Sanjeev Satheesh, Sean Ma, Zhiheng Huang, Andrej Karpathy, Aditya Khosla, Michael Bernstein, et al. ImageNet large scale visual recognition challenge. *IJCV*, 2015. 6
- [39] Soubhik Sanyal, Timo Bolkart, Haiwen Feng, and Michael J Black. Learning to regress 3D face shape and expression from an image without 3D supervision. *CVPR*, 2019. 3, 7
- [40] Matan Sela, Elad Richardson, and Ron Kimmel. Unrestricted facial geometry reconstruction using image-to-image translation. *ICCV*, 2017. 3
- [41] Xiao Sun, Bin Xiao, Fangyin Wei, Shuang Liang, and Yichen Wei. Integral human pose regression. In *ECCV*, 2018. 3, 4, 5
- [42] Ayush Tewari, Michael Zollhofer, Hyeonwoo Kim, Pablo Garrido, Florian Bernard, Patrick Perez, and Christian Theobalt. Mofa: Model-based deep convolutional face autoencoder for unsupervised monocular reconstruction. In *ICCVW*, 2017. 3
- [43] Anh Tuan Tran, Tal Hassner, Iacopo Masi, and Gérard Medioni. Regressing robust and discriminative 3D morphable models with a very deep neural network. In *CVPR*, 2017. 3
- [44] Timo von Marcard, Roberto Henschel, Michael J Black, Bodo Rosenhahn, and Gerard Pons-Moll. Recovering accurate 3D human pose in the wild using IMUs and a moving camera. In *ECCV*, 2018. 7
- [45] Donglai Xiang, Hanbyul Joo, and Yaser Sheikh. Monocular Total Capture: Posing face, body, and hands in the wild. In *CVPR*, 2019. 3, 8
- [46] Bin Xiao, Haiping Wu, and Yichen Wei. Simple baselines for human pose estimation and tracking. In *ECCV*, 2018. 10, 11
- [47] Hongyi Xu, Eduard Gabriel Bazavan, Andrei Zanfir, William T Freeman, Rahul Sukthankar, and Cristian Sminchisescu. GHUM & GHUML: Generative 3D human shape and articulated pose models. In *CVPR*, 2020. 3
- [48] Yi Zhou, Connelly Barnes, Jingwan Lu, Jimei Yang, and Hao Li. On the continuity of rotation representations in neural networks. In *CVPR*, 2019. 6
- [49] Christian Zimmermann, Duygu Ceylan, Jimei Yang, Bryan Russell, Max Argus, and Thomas Brox. FreiHAND: A dataset for markerless capture of hand pose and shape from single RGB images. *ICCV*, 2019. 2, 5, 6, 7, 11